國 立 交 通 大 學

光 電 工 程 研 究 所

碩 士 論 文

Q-開關鎖模雷射照射微結構光纖產生之超連續光譜

Supercontinuum Generation from Microstructured Fibers

by a Q-Switched Mode-Locked Laser

研 究 生：許 展 榕

指 導 教 授：謝 文 峰 教授

中 華 民 國 九 十 五 年 六 月

Q-開關鎖模雷射照射微結構光纖產生之超連續光譜

Supercontinuum Generation from Microstructured Fibers
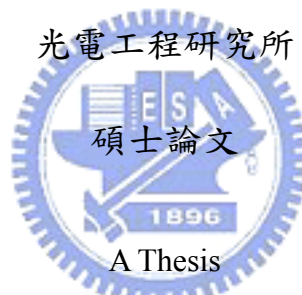
by a Q-Switched Mode-Locked Laser

研 究 生：許展榕 　　　　　Student: Chan-Jung Hsu

指導教授：謝文峰 教授 　　　Advisor: Dr. Wen-Feng Hsieh

國立交通大學

光電工程研究所

碩士論文

中華民國九十五年六月

Q-開關鎖模雷射照射微結構光纖產生之超連續光譜

研究生：許 展 榕　　　　　指導教授：謝 文 峰 教授

國立交通大學光電工程研究所

摘要

　　我們於此篇論文報導了藉由 Q-開關(Q-switched)鎖模脈衝雷射耦合至微結構光纖，在低平均功率底下(220 mW)，產生了 950 nm 至 1450 nm 寬的超連續光譜。微結構光纖具有特殊的色散曲線和很大的非線性係數，因此成為產生超連續光譜的有力材料。而 Q-switched 鎖模脈衝雷射即使在低平均功率底下，仍具有很高的峰值功率，其峰值功率約 CW 鎖模脈衝雷射的 14 倍，因此可以引發各種非線性效應，諸如調制不穩(modulation instability)、受激拉曼散射(Stimulated Raman scattering)和高階色散(higher-order dispersion)等效應，這些效應均是產生超連續光譜的主因。我們將在此篇論文對微結構光纖之非線性效應，作詳盡的解說。另外我們也利用非線性薛丁格方程式來模擬實驗的結果，得到相當好的印證，模擬理論與方式也會在此篇論文作詳細的介紹。

Supercontinuum Generation from Microstructured Fibers by a Q-Switched Mode-Locked Laser

Student: Chan-Jung Hsu   Advisor: Dr. Wen-Feng Hsieh

Institute of Electro-Optical Engineering

National Chiao Tung University

Abstract

In this thesis, we reported the supercontinum generation from 950 nm to 1450 nm by using a Q-switched mode-locked laser coupling to a microstructured fiber under the low pumping average power of 220 mW.   The microstructured fibers have special dispersion curve and high nonlinear coefficient and therefore are a powerful tool to generate supercontinuum.   A Q-switched mode-locked laser has high peak power even with low average power, whose peak power is about 14 times higher than that of the CW mode-locked laser, thus it can easily generate various kinds of nonlinear effects, such as the modulation instability, the stimulated Raman scattering and the higher-order dispersion.   These nonlinear effects are the major causes to generate the supercontinuum.   We will introduce the microstructured fibers and the nonlinear effects thoroughly in this thesis.   We also simulated our experiment results by using the nonlinear Schrödinger equation that shows a great matching.   The theory and the detail simulation will also be demonstrated in this thesis.

致謝

終於來到這一刻，感謝神我終於畢業了！完成人生的一個階段，爸、媽，我會繼續努力的！首先要感謝我的指導教授謝文峰老師，他真的是我到目前為止所知道最鬼才的老師了，老師近乎飛秒級的思考速度與跳躍性的思考模式，讓我有時候懷疑自己與老師是否是同星球的人。再來我要感謝大師兄與家弘學長的指導，除了提供我很多的知識外，也常請我吃飯，學長，謝了！另外也感謝實驗室博班學長姐的照顧：智章學長，謝謝你平常對我大大小小問題的解答。晴如學姐，如果沒有你在，實驗室就沒什麼人能跟我對嗆了，(不要忘了我的馬偕之恩)。還有黃董、維仁、至賢、信民學長，有你們在實驗室就多了許多的安全感。另外楊松學長，妳是我實驗室的拜把，兄弟，妳懂的！小豪學長，以後太陽能搞出來，不要忘記我！國鋒學長，晚上睡覺不要再想公式了！剩下一堆我的學弟妹們，你們真的是我碩士班最快樂的來源：影書，妳是我實驗室唯一的朋友。明容，妳永遠是我心目中那位白雪公主。玫丹，要溫柔點！輝鴻，不要再看無名的女生了，要看也要記得丟給我。郭笨，不要再摸魚了。新翰，妳是我的實驗助教。你們這三劍客，雖然你們都很愛嗆我，但是這些白爛的日子，真的還蠻有趣的，我愛你們！！真的。最後最後，感謝神保守我在研究所的生活，讓我交了這麼多的好朋友，也讓我經歷了好多的事情。親愛的神，希望你也能祝福我在實驗室的弟兄姊妹們，讓他們過一個充實與快樂的學生生活！

展榕

Abstract (in Chinese)
Abstract (in English)
Acknowledgements
Contents
List of Figures
List of Tables

List of Figures

List of Tables

Chapter 1   Introduction

1.1   Photonic Crystal Fibers

The research of photonic crystal fibers (PCFs) started as early as in the 70's [1]. However, its impact was not prominent until the 90's when the technology was able to fabricate the perfect structures of PCFs.   The great flexibility in the design of PCFs led to tremendous progress in various domains such as optical frequency metrology, sensor technology, medical science, and telecommunications [2-6].

Photonic crystal fibers [7-9] can be classified into two categories: microstructured fibers (MFs) and photonic bandgap fibers (PBFs).   Figure 1.1 shows the MF in which its solid core is surrounded by an array of air holes.   Due to its higher refractive index of the core than the cladding, the MF can guide light as the standard fibers by the principle of the total internal reflection.
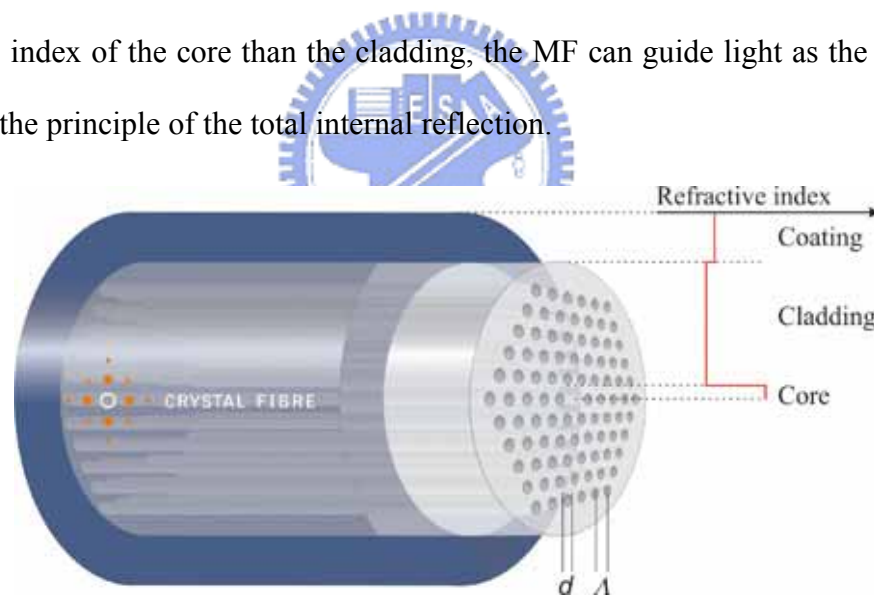
Fig. 1.1   The scheme of the microstructured fiber. d is the diameter of the air holes and Λ is the pitch, the distance between the two air holes.

The dispersion profile of MFs strongly depends on the air-filling fraction and core size.   For example, increasing the air-filling fraction and reducing the size of the core allows for a drastic increase of the waveguide dispersion, thus enabling to shift

the zero-dispersion wavelength of MFs to below 800 nm [10].　The dispersion is then anomalous at visible wavelengths and soliton propagation becomes possible for this range of wavelengths.　A shift of the zero-dispersion wavelength to any value from 500 nm to 1500 nm can be obtained in MFs.　Furthermore, by choosing the appropriate air-hole size and pitch, it is possible to fabricate MFs that exhibit very low and flat dispersion over a relatively broad wavelength range [11-13].

PBFs are the fibers which guide light in their hollow core.　Figure 1.2 shows the scheme of PBFs.　In PBFs, the periodic arrangement of the air holes can be seen as the photonic bandgap structure and their hollow core is the defect inside the structure. The photonic bandgap structure will result in a bandgap which allows only certain range of wavelength exiting in it.　Outside this range, PBFs is anti-guiding. Guiding light in a hollow core holds many promising applications like high power delivery without the risk of fiber damage, gas sensors or extreme low loss guidance in vacuum.　Furthermore, they are almost insensitive to bending (even at very small bending radii) and have extreme dispersion properties, such as anomalous dispersion values in the thousands of ps/nm/km regime are easily obtained.　Due to a negligible contribution from the core material (air), the total dispersion of PBG fibers is to a high degree dominated by waveguide dispersion.
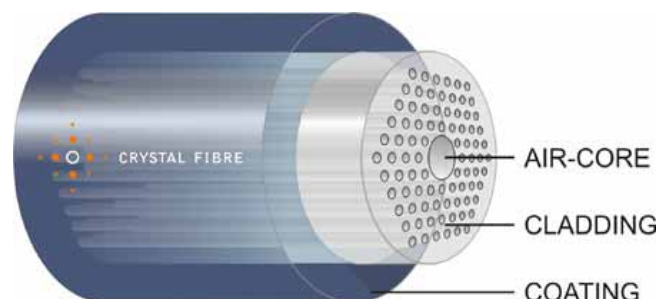
Fig. 1.2　The scheme of photonic bandgap fibers (PBFs).　Light is guided in the air-core of PBFs.

1.2   Supercontinuum Generation

Supercontinuum (SC) generation is formation of broad continuous spectra by propagation of high power pulses through nonlinear media [14]. Provided enough power, SC generation can be observed in a drop of water [15]. However, the nonlinear effects involved in the spectral broadening are highly dependent on the dispersion of the media; and a clever dispersion design can significantly reduce the power required. The widest spectra are obtained when the pump pulses are launched close to the zero-dispersion wavelength of the nonlinear media. Due to the technology which can fabricate the shiftable dispersion profile and small core MFs, MFs become powerful tools to generate the SC and was first demonstrated in 1999 [16]. The zero-dispersion wavelength of MFs can be shifted close to the pumping wavelength and the small core of MFs enhances the nonlinear effects, mechanisms leading to the SC.

To generate the SC with MFs, femtosecond [17][18] and picosecond mode-locked laser systems were generally used as the pumping sources [19]. For femtosecond pumping, it's easily to get higher peak power of the pumping pulse due to its short pulse duration and therefore to induce strong nonlinear effects. These nonlinear effects include high-order soliton breakup [20][21], self-frequency shift [22] and four-wave mixing [23]. Usually about mini-watts of average pumping power are needed to generate the supercontinuum for a femtosecond mode-locked laser system [18]. However, a femtosecond mode-locked laser system is more expensive and complex to build. A picosecond mode-locked laser system is a better way to choose. For picosecond pumping, the major nonlinear effects for spectrum broadening are modulation instability and stimulated Raman scattering if it is pumped in the anomalous dispersion region, where the group-velocity dispersion β_2 is negative. In

2002, Mickael Seefeldt reported the SC from 700 nm to 1600 nm with an average

input power of 5.0 W using passively mode-locked Nd:YVO$_4$ which generated a pulse

width of 10 ps. [19]   Compared with femtosecond pumping, an average power up to

several watts should be needed to generate sufficient supercontinuum for picosecond

pumping.   It is due to its longer duration of pulse width.   Therefore, a higher

average power is necessary to get enough pumping peak power.

1.3   Motivation

To enhance the effect of the SC, a simple way is to increase the pumping peak

power.   In our passively mode-locked Nd:GdVO$_4$ laser system which can generate a

pulse width of 15 ps, the peak power of Q-switched mode-locked (QML) state is

about 14 times higher than that of CW mode-locked state (CML).   We can utilize

this characteristic to strengthen the nonlinear optical effects for the SC.
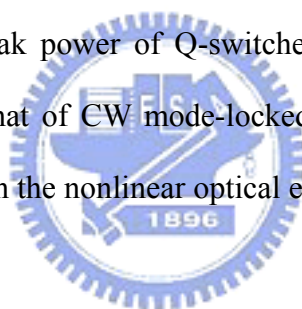
1.4   Organization of this Thesis

In Chapter 2, we will introduce the theory of SC.   The content describes several

nonlinear effects and the nonlinear Schrödinger equation, a general equation

presenting the nonlinear phenomenon.   In Chapter 3, we will describe how to

simulate the nonlinear Schrödinger equation.   Then, we will introduce our

experiment, including the pumping laser system, the specification of our MF and the

experimental setup in Chapter 4.   Chapter 5 is the experiment results and discussion.

We will compare the experiments results with the numerical results in this chapter.

Finally, we will give a conclusion and the future works in Chapter 6.   Appendix will

show how to simulate the dispersion of the fiber using "Mode solutions", software

made by Lumerical.

Chapter 2   Theory of the Supercontinuum Generation

2.1   Nonlinear Optical Effects

Nonlinear effects are the major mechanisms leading to the supercontinuum (SC). With enough peak power, a pulse propagating in the fiber will induce several nonlinear effects.   Under the picosecond pulse pumping in the anomalous dispersion region, a pulse will experience the self-phase modulation (SPM) [21], one of the nonlinear effects leading to the spectral broadening of the pulse.   The nonlinear phase induced by SPM will interact with the anomalous dispersion and generate pairs of new frequencies at each side of pumping.   This phenomenon is what we call modulation instability (MI) [17][21], which can be regarded as degenerate four-wave mixing (DFWM).   Once the new frequencies locate in the spectrum of Raman gain, they will experience the stimulated Raman scattering (SRS) and self-steepening (SS) which shift the spectrum further into longer wavelength and distort the shape of spectrum.   Higher-order dispersion (HOD) (usually β_3 and β_4) should also be considered if the spectrum extends from the anomalous dispersion region to the normal dispersion region [24].   The new dispersive wave will be generated at the normal dispersion region.   Those nonlinear effects mentioned above will be described more detail in the following.

2.1.1   Self-phase Modulation

SPM is a phenomenon that leads to spectral broadening of optical pulses.   It originates from the intensity-dependence of the refractive index [25]:

$$n = n_L + n_2 |A|^2 ,$$
(2.1.1)

where n_L is the linear part of the refractive index, n_2 is the nonlinear index coefficient

and $|A|^2$ is the optical intensity. A typical value of n_2 for silica material is 3.2×10^{-20} m^2/W. For an optical pulse, SPM refers to the self-induced nonlinear phase shift as it propagates along the fiber

$$\phi_{NL}^{SPM}(T) = \frac{2\pi L}{\lambda} n_2 |A(T)|^2 , \quad (2.1.2)$$

where L is the length of the fiber. This nonlinear phase shift can induce a frequency chirp which leads to the spectral broadening of the pulse. A useful quantity γP_p interprets the maximum nonlinear phase shift for a pulse propagating in fibers, where P_p is the peak power of the optical pulse and γ is the nonlinear coefficient [21]

$$\gamma = \frac{n_2 \omega}{c A_{eff}} . \quad (2.1.3)$$

Here A_{eff} is the effective area of the propagating mode inside the fiber and ω is the center frequency of the optical field. The nonlinear coefficient γ represents the strength of nonlinear effects and is inversely proportional to the area of fiber core.

2.1.2   Degenerate Four-Wave Mixing

DFWM is a process where two pump photons generate a Stokes photon and an anti-Stokes photon:

$$2\omega_p \rightarrow \omega_s + \omega_{as} , \quad (2.1.4)$$

where ω_p, ω_s and ω_{as} correspond to the pump, Stokes, and anti-Stokes frequencies, respectively. Being a coherent process, four-wave mixing is efficient only if the phase-matching condition is fulfilled [18], i.e.,

$$\Delta\phi = \phi(\omega_s) + \phi(\omega_{as}) - 2\phi(\omega_p) = L\left[2\sum_n \frac{\beta_{2n}}{(2n!)}(\omega_s - \omega_p)^{2n} + 2\gamma P_p\right] = 0 . \quad (2.1.5)$$

7

Here β_{2n} is the $2n^{th}$ derivative of the propagation constant β with respect to the frequency. Note that only the even terms of the series expansion of β contribute to the phase-matching condition and the odd terms will cancel one another. The nonlinear phase shift $2\gamma P_p$ due to SPM should be also included in the phase-matching condition. For a pump wavelength located in the anomalous dispersion region, the phase-matching condition is mainly governed by the induced nonlinear phase shift. Usually the process of DFWM in the anomalous region can be regarded as MI which we will discuss in next section.

2.1.3 Modulation Instability

For a pump wavelength located in the anomalous dispersion region, it is possible to compensate the induced nonlinear phase shift $2\gamma P_p$ by the negative value of β_2 and generate the corresponding Stokes and anti-Stokes components. The frequency difference between the pump and the Stokes (anti-Stokes) component calculated by Eq. 2.1.5 is [21]

$$\Omega_s = \pm \left(\frac{2\gamma P_p}{|\beta_2|} \right)^{\frac{1}{2}}, \tag{2.1.6}$$

if considering only the term of β_2. This frequency shift can also be calculated by solving the standard nonlinear Schrödinger equation (NSE) of CW light [21]. By using the perturbation theory, the CW light solution of NSE will become unstable in the anomalous dispersion region and generate two new frequencies on ether side of the pump frequency. These two new frequencies calculated by perturbation of CW solution are as the same as the frequencies calculated by the DFWM. The new frequencies will break up the CW or quasi-CW radiation into a train of ultra short

pulses. We call this phenomenon MI which results from an interplay between the nonlinear and the dispersive effects. In fact, MI can be interpreted in terms of DFWM in the frequency domain, whereas in the time domain it results from an unstable growth of weak perturbation from the CW steady state.

2.1.4 Stimulated Raman Scattering

SRS is a photon-phonon interaction. It is described quantum-mechanically as scattering of a photon by one of the molecules to a lower -frequency photon, while the molecule makes transition to a higher energy vibrational state. SRS can yield gain for a probe wave co-propagating with a pump wave and whose wavelength is located within the Raman gain bandwidth. The normalized Raman gain spectrum of silica is shown in Fig. 2.1 as a function of frequency difference between the pump and probe waves [26]. The Raman gain of the MFs is comparable to that of silica fibers [27]. The gain bandwidth is 40 THz with a peak located at 13.2 THz from the pump frequency. For an ultra-short pulse, the spectral width of the pulse is large enough that the Raman gain can amplify the low-frequency (red) spectral components of the pulse, with high-frequency (blue) components of the same pulse acting as a pump. This effect is called intrapulse Raman scattering [21]. As a result, the pulse spectrum shifts toward the low-frequency (red) side as the pulse propagates inside the fiber, a phenomenon referred to as the self-frequency shift.
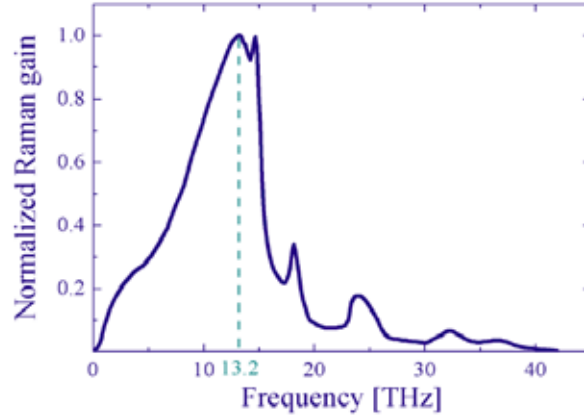
Fig. 2.1   Raman-gain spectrum for fused silica at a pump wavelength $\lambda_p = 1$ μm.

2.1.5   Self-Steepening

Self-steepening (SS) results from the dispersion of the third-order susceptibility, i.e.,
the red frequency components experience a lower nonlinearity than the blue
frequency components.   In the time domain, SS can be thought as the intensity
dependence of the group velocity: the peak of the pulse moves at a slower velocity
than the wings which induces the trailing edge of the pulse to become steeper as the
pulse propagates [21].   In combination with SPM, SS results in a more pronounced
broadening of the blue frequency components compared to the red ones.   The
process of self-frequency shift is substantially reduced by SS since the nonlinearity
decreases as the center wavelength of the soliton shifts towards the red.

2.1.6   Higher-order Dispersion

Higher-order dispersion (HOD) effect becomes important in optical fibers when the
carrier frequency is close to the zero dispersion point.   Once the spectrum extends
beyond the zero dispersion point to the normal dispersion region, the spectrum will be
disturbed by the HOD to generate a new dispersive wave [See Fig 2.2].   This is
because when accounting the higher-order dispersion, the wavenumber of the

10

propagating pulse is the same as the dispersive wave so that the energy can transfer

from the pulse to the dispersive wave.
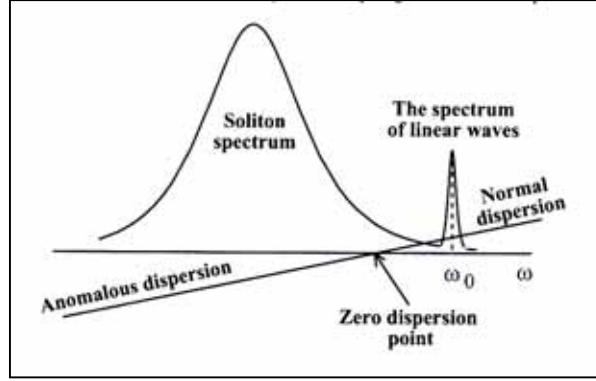
Fig. 2.2   The dispersive wave generated at the normal dispersion due to the

perturbation of HOD [24].

2.2 Nonlinear Schrödinger Equation

An electromagnetic field propagating in a medium induces a polarization of the

electric dipoles.   The evolution of the electromagnetic field in the medium can be

described by a propagation equation derived from the general wave equation [21]

$$\nabla^2 E - \frac{1}{c^2}\frac{\partial^2 E}{\partial t^2} = \mu_0 \frac{\partial^2 P}{\partial t^2},$$ (2.2.1)

where E is the electric field, P the induced polarization, μ_0 the vacuum permeability

and c the speed of light in vacuum.   For intense radiation such as laser pulses, the

response of the medium becomes nonlinear and the induced polarization consists of a

linear and a nonlinear parts.   In the scalar approximation, the linear and nonlinear

induced polarizations are related to the electromagnetic field as [21]

$$P_L = \varepsilon_0 \chi^{(1)} E,$$ (2.2.2)

$$P_L = \varepsilon_0 \sum_{j\geq 2} \chi^{(j)} E^j,$$ (2.2.3)

11

where ε_0 is the vacuum permittivity and $\chi^{(j)}$ is the jth order susceptibility of the medium. The inversion symmetry of silica glass at the molecular level results in negligible even-order susceptibilities. Moreover, susceptibilities of order higher than 3 are not significant for silica glass. Therefore, the relevant nonlinear effects in optical fibers are mainly induced by $\chi^{(3)}$ [21].

Optical nonlinear processes can be divided in two categories. Elastic processes correspond to photon-photon interaction with no energy exchange occurring between the electric field and the medium. Such effects include SPM, DFWM, and generation of dispersive wave. Inelastic processes correspond to photon-phonon interaction, which leads to energy exchange between the electric field and the nonlinear medium. Raman scattering is one of the effects of inelastic process. Treating the nonlinear part of the induced polarization as a perturbation in Eq. 2.2.1 and assuming that the electric field is of the form

$$E(z,T) = A(z,T)\exp(i\beta z - i\omega_0 T), \qquad (2.2.4)$$

where $A(z,T)$ is the slowly varying envelope of the electric field, β is the propagation constant and ω_0 is the center frequency of the field, one can derive the well-known NSE. The NSE models accurately the propagation of light along optical fibers for pulses as short as 30 fs [28]. In a frame of reference moving at the group velocity of the pulse, the NSE can be written as [21]

$$\frac{\partial A}{\partial z} + \frac{\alpha}{2} - \sum_{n \geq 2} \frac{i^{n+1}}{n!} \beta_n \frac{\partial^n A}{\partial T^n} = i\gamma(1 + \frac{i}{\omega_0}\frac{\partial}{\partial T})A \int_{-\infty}^{+\infty} R(T')\left|A(z,T-T')\right|^2 dT', \quad (2.2.3)$$

where α is the fiber loss and β_n are the coefficients of the Taylor-series expansion of the propagation constant β around ω_0, and $R(T)$ is the response function describing the interaction between the photon and medium. The response function should include

both the instantaneous response (interaction between electron and photon) and the delayed Raman response (interaction between photon and phonon) and is given by

$$R(T) = (1 - f_R)\delta(T) + f_R h_R(T),$$ (2.2.4)

where f_R represents the fractional contribution of the delayed Raman response function $h_R(T)$. The value of f_R is typically 0.18 and $h_R(T)$ can be presented as [300]

$$h_R(T) = \frac{\tau_1^2 + \tau_2^2}{\tau_1 \tau_2^2} e^{-\frac{T}{\tau_2}} \sin(\frac{T}{\tau_1})$$ (2.2.5)

where $\tau_1 = 12.2$ fs and $\tau_2 = 32$ fs. Figure 2.3 shows the temporal variation of $h_R(T)$ [29]. The delayed Raman response $h_R(T)$ can describe the phenomenon of intrapulse Raman scattering referred to the self-frequency shift. The right-hand side of Eq. 2.2.3 contains the nonlinear effects such as SPM, intrapulse Raman scattering and SS, the differential term which accounts for the dispersion of the nonlinear coefficient. On the left side of the Eq. 2.2.3, it presents not only the dispersion effect but also the fiber loss. By simulating the NLS, we can get the evolution of an optical pulse propagating in fibers and therefore realize the causes of the SC.
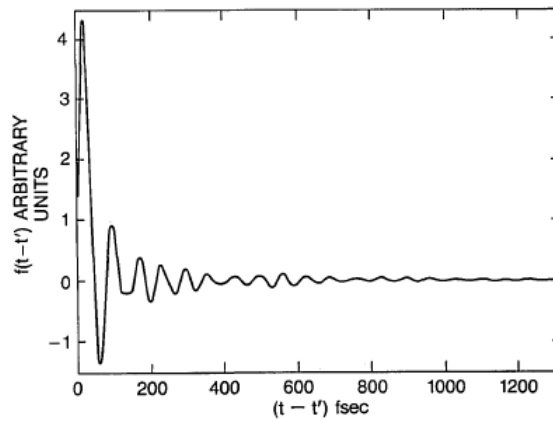

Fig. 2.3 Temporal variation of delayed Raman response function $h_R(T)$ for silica fibers [28].

Chapter 3   Simulation Methods

3.1   Simulation of the Nonlinear Schrödinger Equation

The NSE is an important tool to analyze the evolution of a pulse propagating in fibers.   By solving the NSE, we can get the final spectrum of the pulse out of the fiber.   In general, the NSE is a nonlinear partial differential equation and doesn't have an analytic solution.   A numerical approach is therefore often necessary for understanding the nonlinear effects in optical fibers.   A large number of numerical methods can be used for this purpose.   These can be classified into two broad categories known as: (i) the finite-difference methods and (ii) the pseudospecral methods.   Generally speaking, pseudospecral methods are faster by up to an order of magnitude to achieve the same accuracy [30].   It has been used extensively to solve the pulse-propagation problem in nonlinear dispersive media is the split-step Fourier method [31] [32].

In this thesis, we solve the NSE using the split-step Fourier method.   Other concepts such as the discrete Fourier transform (DFT), fast Fourier transform (FFT) and convolution theory should also be used in the simulation of NSE.   In this chapter, we will introduce the DFT, FFT and the convolution theory from 3.1.1 to 3.1.3. Then we will show how to use these tools to solve NSE by the split-step Fourier method in detail in 3.2

3.1.1   Discrete Fourier Transform

A physical process can be described in the time domain t and the frequency domain f as functions of $h(t)$ and $H(f)$ respectively.   For many purposes it is useful to think $h(t)$ and $H(f)$ as being two different representations of a physical process.   One goes back and forth between these two representations by means of the Fourier transform.

We can get $H(f)$ by the Fourier transform of $h(t)$ or $h(t)$ by the inverse Fourier transform of $H(f)$ [33] .

$$H(f) = \int_{-\infty}^{\infty} h(t)e^{2\pi i f t}dt, \qquad (3.1.1)$$

$$h(t) = \int_{-\infty}^{\infty} H(f)e^{-2\pi i f t}df. \qquad (3.1.2)$$

In the most computational work, the function we deal is usually a train of sampled data at evenly spaced intervals in time.   If we sample a continuous function $h(t)$ to N consecutive values, $h(t)$ can be presented as

$$h_k \equiv h(t_k), \qquad t_k \equiv k\Delta, \qquad k = 0, 1, 2, \ldots, N - 1, \qquad (3.1.3)$$

where Δ is the time interval.   According to the sampling theory, a continuous function $h(t)$, sampled at an interval Δ, happens to be bandwidth limited to frequencies from $-f_c$ to f_c where $f_c = 1/2\Delta$ [33].   Let us sample the frequency to N consecutive values inside the bandwidth, i.e.,

$$f_n \equiv \frac{n}{N\Delta}, \qquad n = -\frac{N}{2} \ldots, \frac{N}{2}, \qquad (3.1.4)$$

where N is usually taken as an even number.   If we really count the number of f_n, we will find that there are $N+1$ values of n.   It turns out that the two extreme values of n are not independent (in fact they are equal), but all the others are.   This reduces the count to N.

We can approximate the integral in Eq. 3.1.1 by a discrete sum [33]:

$$H(f_n) = \int_{-\infty}^{\infty} h(t)e^{2\pi i f t}dt \approx \sum_{k=0}^{N-1} h_k e^{2\pi i f_n t_k}\Delta = \Delta\sum_{k=0}^{N-1} h_k e^{2\pi i k n/N}. \qquad (3.1.5)$$

The final summation in Eq. 3.1.5 is called the DFT of the N points of h_k.   Let us denote it as function H_n,

$$H_n = \sum_{k=0}^{N-1} h_k e^{2\pi i k n / N} \ . \tag{3.1.6}$$

The relation between the DFT and continuous Fourier transform with a continuous function sampled at an interval Δ can be written as

$$H(f_n) \approx H_n \tag{3.1.7}$$

From Eq. 3.1.4, we have seen that the index n varies from $-N/2$ to $N/2$. However, we find that Eq. 3.1.6 is periodic in n with period N. Therefore, $H_{-n} = H_{N-n}$, where $n = 1, 2, ...$ With this conversion, we let H_n for n from 0 to N-1 form one complete period. When this convention is followed, we must remember that the zero frequency corresponds to $n = 0$, positive frequencies $0 < f < f_c$ correspond to values $1 \le n \le N/2-1$, while negative frequencies $-f_c < f < 0$ correspond to $N/2+1 \le n \le N-1$. The value $n = N/2$ corresponds to *both* $f = f_c$ and $f = -f_c$ [33].

The formula for the discrete inverse Fourier transform, which recovers the set of h_k's exactly from the H_n's is [33]:

$$h_k = \frac{1}{N} \sum_{n=0}^{N-1} H_n e^{-2\pi i k n / N} \ . \tag{3.1.8}$$

Notice that there are only two differences between Eq. 3.1.6 and Eq. 3.1.8. One is changing sign in the exponential and the other is further dividing by N. This means that a routine for calculating the DFT can also be used, with slight modification, to calculate the inverse transform.

3.1.2   Fast Fourier Transform

How much computation work is needed to compute the DFT? Let us introduce a new complex number W:
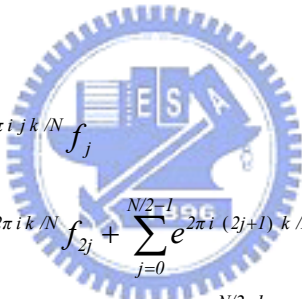
$$W \equiv e^{2\pi i / N}, \tag{3.1.9}$$

then Eq. 3.1.6 can be written as [33]

$$H_n = \sum_{k=0}^{N-1} W^{nk} h^k .$$ (3.1.10)

The vector h_k is multiplied by a matrix W of the power $n \times k$. This matrix multiplication finally requires N^2 complex multiplications, plus a smaller number of operations to generate the required powers of W. So, the DFT appears to be an order of N^2 processes. However, the computation work can be reduced to an order of $N \log_2 N$ by means of FFT. The difference between N^2 and $N \log_2 N$ is huge for large N. For a microsecond time computer, it takes 2 weeks to finish N^2 computation whereas only 30 seconds for $N \log_2 N$ for $N=10^6$.

The DFT of length N can be rewritten as the sum of two DFTs, each of length $N/2$. One of the two is formed from the even-numbered points of original N, the other from the odd-numbered points [33].

$$
\begin{aligned}
F_k &= \sum_{j=0}^{N-1} e^{2\pi i j k /N} f_j \\
&= \sum_{j=0}^{N/2-1} e^{2\pi i k /N} f_{2j} + \sum_{j=0}^{N/2-1} e^{2\pi i \, (2j+1) \, k /N} f_{2j+1} \\
&= \sum_{j=0}^{N/2-1} e^{2\pi i j k /(N/2)} f_{2j} + W^k \sum_{j=0}^{N/2-1} e^{2\pi i j k /(N/2)} f_{2j+1} \\
&= F_k^e + W^k F_k^o
\end{aligned}
$$ (3.1.11)

F_k^e denotes the kth component of the Fourier transform of length $N/2$ formed from the even components, while F_k^o is the corresponding transform of length $N/2$ formed from the odd components. The dichotomy of the DFT can be used recursively. We can do the same reduction of F_k^e to the two DFTs, each of length $N/4$. In other words, we can define F_k^{ee} and F_k^{eo} to be the DFTs of the points which are respectively even-even and even-odd on the successive subdivisions of the data. If we treat N as an integer power of 2, it is evident that we can continue applying the

17

dichotomy until we have subdivided the data all the way down to transforms of length 1.

$$F_k^{eoeeoeo...ee} = f_k \qquad \text{for some n.} \qquad (3.1.12)$$

From Eq. 3.1.12, we can see that for every pattern of $\log_2 N$ e's and o's, there is a one-point transform that is just one of the input numbers f_n. The final step is to figure out which value of n corresponds to which pattern of e's and o's in Eq. 3.1.12. By using this information, we can calculate F_k. This is what we call the FFT.

In our simulation, we use Compaq Visual Fortran 6.6. In the library of Compaq Visual Fortran 6.6, the instructions of the FFT and the inverse FFT are DFFTCF and DFFTCB. The output of DFFTCF is H_n. That means we need to multiply the output by the interval Δ to get the Fourier transform $H(f_n)$. For DFFTCB, the output should be divided the sampled number N to get h_k as Eq. 3.1.8. We should also notice that the sampled number N, the input in DFFTCF and DFFTCB, should be an integer of the power of 2.
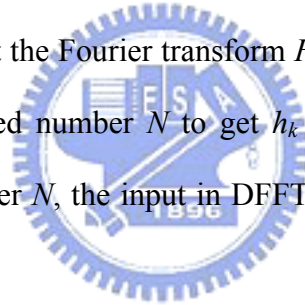
3.1.3 Convolution Theory

A system is said to be linear if it satisfies the principle of superposition, i.e., if its response to the sum of any two inputs is the sum of its responses to each of the inputs separately. The output at time t is, in general, a weighted superposition of the input contributions at difference time τ [34],

$$f_2(t) = \int_{-\infty}^{\infty} h(t;\tau) f_1(\tau) d\tau , \qquad (3.1.13)$$

where $f_1(t)$, $f_2(t)$ and $h(t;\tau)$ are the input, the output of the linear system and a weighting function representing the contribution of the input at time τ to the output at

time t, respectively.

A linear system is said to be **time-invariant** or **shift-invariant,** if when the input of a linear system is shifted in time, its output shifts by an equal time, but otherwise remains the same. Then $h(t; \tau)$ can be written as $h(t - \tau)$ and Eq. 3.1.13 becomes [34]

$$f_2(t) = \int_{-\infty}^{\infty} h(t - \tau) f_1(\tau) d\tau . \qquad (3.1.13)$$

The Fourier transform of $f_2(t)$ is the product of the Fourier transform of $h(t - \tau)$ and $f_1(t)$. This is known as the convolution theory presented as [34]

$$F_2(\nu) = H(\nu) F_1(\nu), \qquad (3.1.14)$$

where $F_1(\nu)$, $F_2(\nu)$ and $H(\nu)$ are the Fourier transform of $f_1(t)$, $f_2(t)$ and $h(t; \tau)$. In the NSE, the response function $R(T)$ can be treated as $h(t - \tau)$ and thus we can calculated the integral part in NSE by the inverse Fourier transform of Eq. 3.1.14.

3.2 Split-step Fourier method

One of the pseudospecral methods that have been used extensively to solve the pulse-propagation problem in nonlinear dispersive media is the split-step Fourier method. The main reason for the faster speed of the split-step method compared with the most finite-difference schemes is the use of the FFT.

To understand the philosophy behind the split-step Fourier method, it is useful to rewrite Eq. 2.2.3 in the form [21]

$$\frac{\partial A}{\partial z} = \left(\hat{D} + \hat{N} \right) A, \qquad (3.2.1)$$

where $\hat{D}$ is a differential operator that accounts for the dispersion and absorption in a media and $\hat{N}$ is a nonlinear operator that presents the effect of fiber nonlinearities on pulse propagation. These operators are given by [21]

$$\hat{D} = \frac{\alpha}{2} - \sum_{n \geq 2} \frac{i^{n+1}}{n!} \beta_n , \qquad (3.2.2)$$

$$\hat{N} = \frac{1}{A} \left\{ i\gamma \left(1 + \frac{i}{\omega_0} \right) \frac{\partial}{\partial T} A \int_{-\infty}^{+\infty} R(T') |A(z,T-T')|^2 dT' \right\} . \qquad (3.2.3)$$

In general, the dispersion and nonlinearity effects act together along the length of the fiber. The split-step Fourier method assumes that the dispersive and nonlinear effects can be pretended to act independently inside a small distance h and therefore obtains an approximation solution. More specifically, propagation along the fiber from the position z to $z + h$ is carried out in two steps. In the first step, the nonlinearity acts alone, and $\hat{D}=0$ in Eq. 3.2.1. In the second step, dispersion acts alone, and $\hat{N}=0$. Mathematically [21],

$$A(z+h,T) \approx \exp(h\hat{D}) \exp(h\hat{N}) A(z,T) . \qquad (3.2.4)$$

The first step can be evaluated in the time domain while the second step should be calculated in the frequency domain. The process is shown as the following prescription

$$A(z+h,T) \approx F_T^{-1} \left(\exp[h\hat{D}(i\omega)] * F_T[\exp(h\hat{N})A(z,T)] \right) \qquad (3.2.5)$$

where F_T, F_T^{-1}, $\hat{D}(i\omega)$ are the FFT operation, the inverse FFT operation and the Fourier transform of $\hat{D}$ in Eq. 3.2.5. Notice that the differential operator $\partial/\partial T$ in $\hat{D}$ can be replaced by $i\omega$, just a number in the frequency domain. That's the reason why the dispersion effect should be calculated in the frequency space. After finishing the dispersion effect on $A(z,T)$, we should change the calculation from the frequency domain to the time domain by the inverse FFT. The use of the FFT makes numerical evaluation of Eq. 3.2.5 relatively fast. It is for this reason that the split-step Fourier method is faster up to two orders of magnitude compared with most of the finite-difference schemes.

To estimate the accuracy of the split-step Fourier method, we note that a formally exact solution of Eq. 3.2.1 is given by

$$A(z+h,T) \approx \exp[h(\hat{D}+\hat{N})]\,A(z,T), \qquad (3.2.6)$$

if $\hat{N}$ is assumed to be z independent.   At this point, it is useful to recall the Baker -Hausdorff formula [35] for two noncommutating operators $\hat{a}$ and $\hat{b}$,

$$\exp(\hat{a})\exp(\hat{b}) = \exp(a+b+\frac{1}{2}[\hat{a},\hat{b}]+\frac{1}{12}[\hat{a}-\hat{b},[\hat{a},\hat{b}]]+....\qquad (3.2.7)$$

where $[\hat{a},\hat{b}] = \hat{a}\hat{b}-\hat{b}\hat{a}$.   A comparison of Eq. 3.2.4 and Eq. 3.2.6 shows that the split-step Fourier method ignores the noncommutating feature of the operators $\hat{D}$ and $\hat{N}$.   By using Eq. 3.2.7 with $\hat{a}=h\hat{D}$ and $\hat{b}=h\hat{N}$, the dominant error term is found resulting from the single commutator $\frac{1}{2}h^2[\hat{D},\hat{N}]$.   Thus, the split-step Fourier method is accurate to the second order in the step size h.

The accuracy of the split-step method can be improved by adopting a different procedure to propagate the optical pulse over one segment from z to $z+h$.   In this procedure Eq. 3.2.4 is replaced by

$$A(z+h,T) \approx \exp(\frac{h}{2}\hat{D})\exp(\int_{z}^{z+h}\hat{N}(z')\,dz')\exp(\frac{h}{2}\hat{D})A(z,T) \qquad (3.2.8)$$

The procedure divides into 3 parts [See Fig. 3.1].   At first, the dispersion effect acts alone in the first half of distance h.   Then the effect of nonlinearity acts alone in the middle of segment.   Finally the dispersion effect acts again in the rest of length $h/2$. Similar to Eq. 3.2.5, the dispersion effects at the both sides of the segment is calculated in the frequency domain by the FFT whereas the nonlinear effect at the middle part is calculated in time domain.
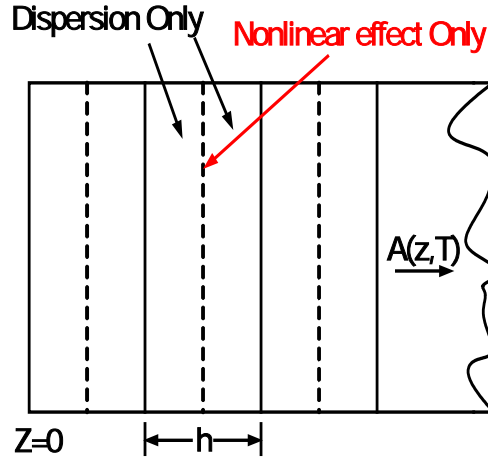
Fig. 3.1   Schematic illustration of the symmetrized split-step Fourier method.   Fiber length is divided into a large number of segments of width *h*.   Within the segment, the effect of nonlinearity acts at the midplane shown by a dashed line.

Because of the symmetric form of Eq. 3.2.8, this scheme is known as the symmetrized split-step Fourier method [36].   The integral in the middle exponential considers the *z* dependent of the nonlinear operator $\hat{N}$.   If the step size *h* is small enough, the integral can be approximated by $\exp(h\hat{N})$.   The most important advantage of using the symmetrized form of Eq. 3.2.8 is that the leading error term comes from the double commutator in Eq. 3.2.7 is of the third order in the step size *h*. This can be proved by applying Eq. 3.2.8 twice in Eq. 3.2.7.

The accuracy of the symmetrized split-step Fourier method can be further improved by evaluating the integral in Eq. 3.2.8 more accurately than approximating it by $h\hat{N}(z)$.   A simple approach is to employ the trapezoidal rule and approximate the integral by [37]

$$\int_{z}^{z+h} \hat{N}(z^{'})\, dz^{'} \approx \frac{h}{2}[\hat{N}(z) + \hat{N}(z+h)] \qquad (3.2.9)$$

22

However, the implementation of Eq. 3.2.9 is not simple because $\hat{N}(z+h)$ is unknown at the mid-segment located at $z+h/2$. It is necessary to use an iterative procedure that is initiated by replacing $\hat{N}(z+h)$ by $\hat{N}(z)$. Equation is than used to estimate $A(z+h,T)$ which in turn is used to calculate the new value of $\hat{N}(z+h)$. Although the iteration procedure is time-consuming, it can still reduce the overall computing time if the step size h can be increased because of the improved accuracy of the numerical algorithm. Two iterations are generally enough in practice.

Let us see Eq. 3.2.3 again, the nonlinear operator $\hat{N}$ contains an integral part and the differential part which corresponds to the Raman effect and the SS. It is more complicated to deal with them. We rewrite $\hat{N}$ by using Eq. 2.2.4 and Eq. 3.2.3 as the following form:

$$
\hat{N} = i\gamma\left((1-f_R)|A(z,T)|^2 + f_R \int_{-\infty}^{+\infty} h_R(T)|A(z,T)|^2 dT' \right)
$$
$$
- \frac{1}{A}\frac{\gamma}{\omega_0}\frac{\partial}{\partial T}\left\{ A\left((1-f_R)|A(z,T)|^2 + f_R\int_{-\infty}^{+\infty} h_R(T')|A(z,T-T')|^2 dT' \right) \right\} . \quad (3.2.10)
$$

The integral part can be solved by the convolution theory by inversely FFT the product of $h_R(\Omega)$ (the FFT of $h_R(T)$) and the FFT of $|A(z,T)|^2$ [38]. The differential part can be solved in the frequency domain by replacing $\partial/\partial T$ with $i\omega$. Therefore, $\hat{N}$ can be written as

$$
\hat{N} = i\gamma X - \frac{\gamma}{\omega_0}\left(\frac{X}{A}F_T^{-1}[i\omega F_T[A]] + F_T^{-1}[i\omega F_T[X]] \right), \quad (3.2.11)
$$

where $X = \left\{ (1-f_R)|A(z,T)|^2 + f_R F_T^{-1}[h_R(\Omega)F_T[|A(z,T)|^2]] \right\}$. Finally, we can compute the nonlinear operator $\hat{N}$ in use of the convolution theory and the FFT algorithm. In many papers, it is usually solved the SS term using the Runge-Kutta method with treating the differential term as a perturbation [33][38][39]. However, we use the

FFT algorithm, which is simpler and more straightforward than the Runge-Kutta method. We therefore simulate the evolution of the pulse spectrum using the split-step Fourier method. We also combine the plug-in program Matfor 4.0 with Compaq Visual Fortran 6.6. Matfor is a very powerful tool which can draft the evolution of spectrum synchronously [Fig. 3.2].
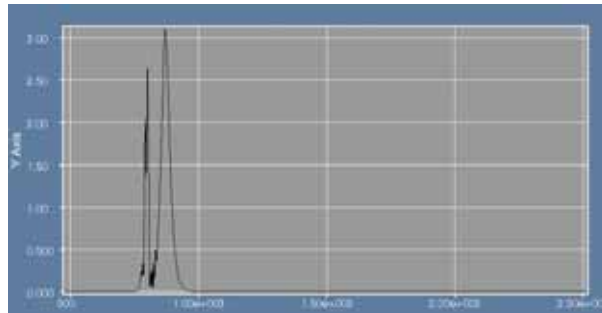

Fig. 3.2   The plug-in program Matfor 4.0

Chapter 4 Experiments

4.1 Pumping Source

Our pumping source, the passively mode-locked $Nd:GdVO_4$ laser, can generate picosecond pulses about 15 ps (FWHM) at the wavelength of 1062.9 nm.   The setup is shown in Figure 4.1.   The laser system is pumped by a diode laser with the maximum power up to 16 W.   The gain medium $Nd:GdVO_4$ has broader emission bandwidth (1.25 nm) and higher thermal conductivity (11.7 W/m*K) than $Nd:YVO_4$ (0.8nm, 5.1W/m*K), thus can generate narrow pulse at high pumping power.   We also use the semiconductor saturable absorber mirror (SESAM) as the saturable absorber.   The SESAM in the laser system is used to generate the CML state and QML state.   With increasing pumping power of diode laser, the laser will be transformed from the CW state to QML state and finally CML state.   Therefore, the average power of CML state is a little bit higher than that of QML state.   At CML state, the laser produces mode-locked pulses at a repetition rate of 126 MHz.   At QML state, the laser produces 1 μs (FWHM) wave packet at a repetition rate of 83.3 kHz [see Fig. 4.2].   There are about 100 CML peaks inside the wave packet.
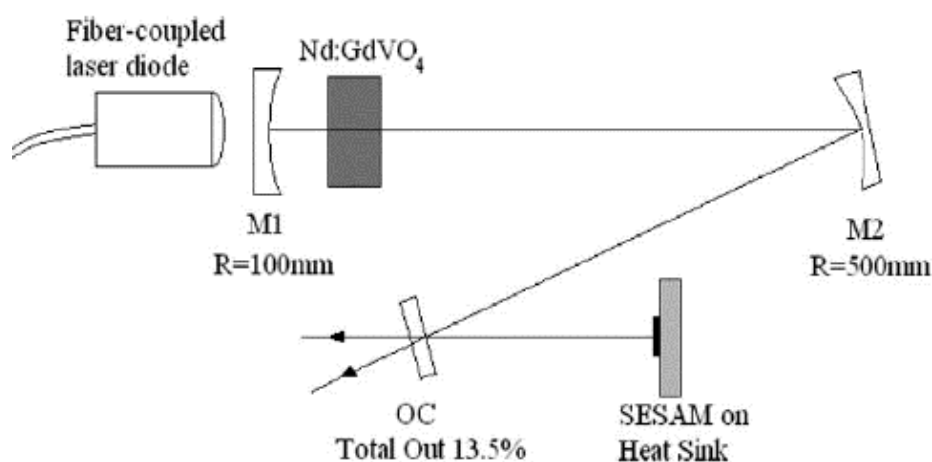

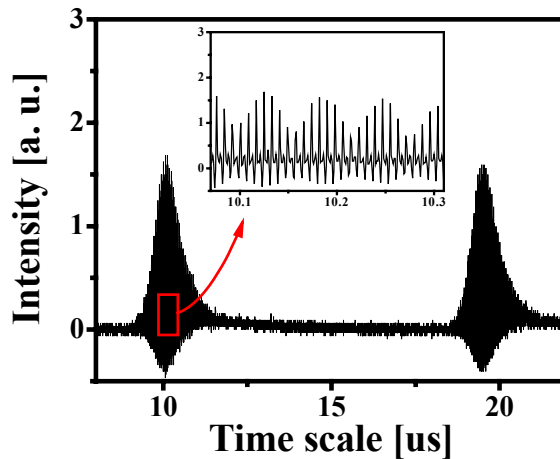Fig. 4.1   The setup of passively mode-locked $Nd:GdVO_4$ laser

Fig. 4.2 The QML pulse trains. The inset is its mode-locked pulses inside the QML pulse. There are about 100 mode-locked pulses inside QML pulse.

4.2 The Specification of the Microstructured Fiber

The core diameter of the used microstructured fiber is about 1.7 μm and the pitch Λ (spacing between adjacent holes) is about 1.4 μm. The diameter of holes is about 0.6μm except for the two holes near the core whose diameter is about 0.7μm. The cross sectional scanning electron microscope image (SEM) of our MF is shown in Fig. 4.3. This fiber has quite high nonlinearity with nonlinear coefficient γ being 74 $km^{-1} \cdot W^{-1}$ due to its small core diameter. It is also polarization maintaining because of its asymmetric arrangement of the holes near the core. It also has two zero dispersion points which are located at 760 nm and 1160 nm. The used pump wavelength is in the anomalous dispersion region. The dispersion curve can be simulated by *Mode Solutions*, software which can calculate frequency-dependent properties of MFs by importing the structures (SEM) of MFs. We will show the result in 5.1.
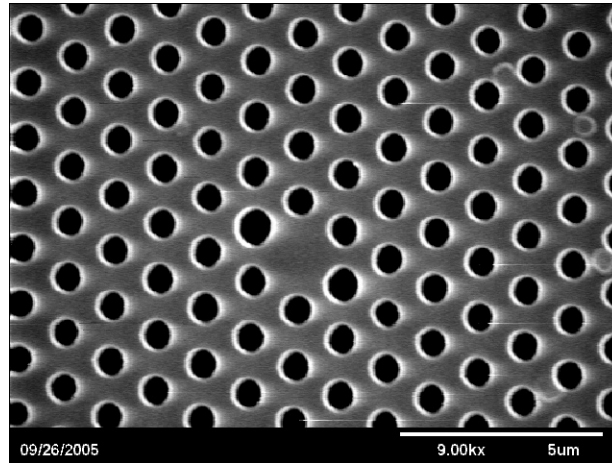
Fig. 4.3　The cross sectional scanning electron microscope image (SEM) of the microstructured fiber.

4.3　Experimental Setup

　In our experiment, the pumping source, passively mode-locked Nd:GdVO$_4$ laser, is focused into a 1-m-long MF with about 35% couple efficiency by a 40X microscope objective lens.　The experiment setup is shown in Fig. 4.4.　A $\lambda/2$ plate is used to change the polarization state of the laser to get the widest spectral broadening.　Finally we measured the output spectrum using an optical spectrum analyzer (OSA).
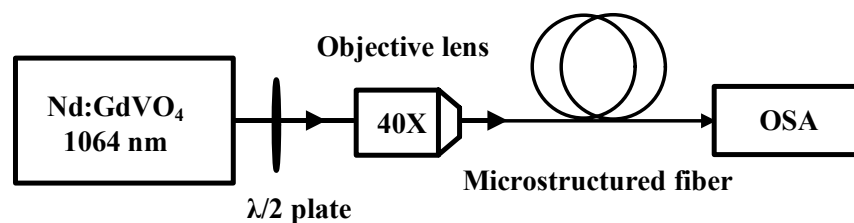

Fig. 4.4　The setup of our experiment.

Chapter 5　Results and Discussion

5.1　Simulated Dispersion Curve of the Microstructured Fiber

By the *Mode Solutions* mentioned in Chapter 4.2, we obtained the simulated dispersion curve and the mode pattern of our MF which are shown in Fig. 5.1. Our simulation result shows that the two zero-dispersion points are located at 790 nm and 1190 nm which slightly different from the provide specification from the suppler. This may be due to the distortion of SEM, the shadows around the air holes. The shadows will influence the calculation of real size of air holes. However, our simulation result of the SC which will be shown in **Fig. 5.3** is quite similar to the experiment result when using the parameters of the simulated dispersion curve. The parameters of the dispersion (including the higher order dispersion up to β_6) at the 1062.9 nm are shown in Table 5.1.
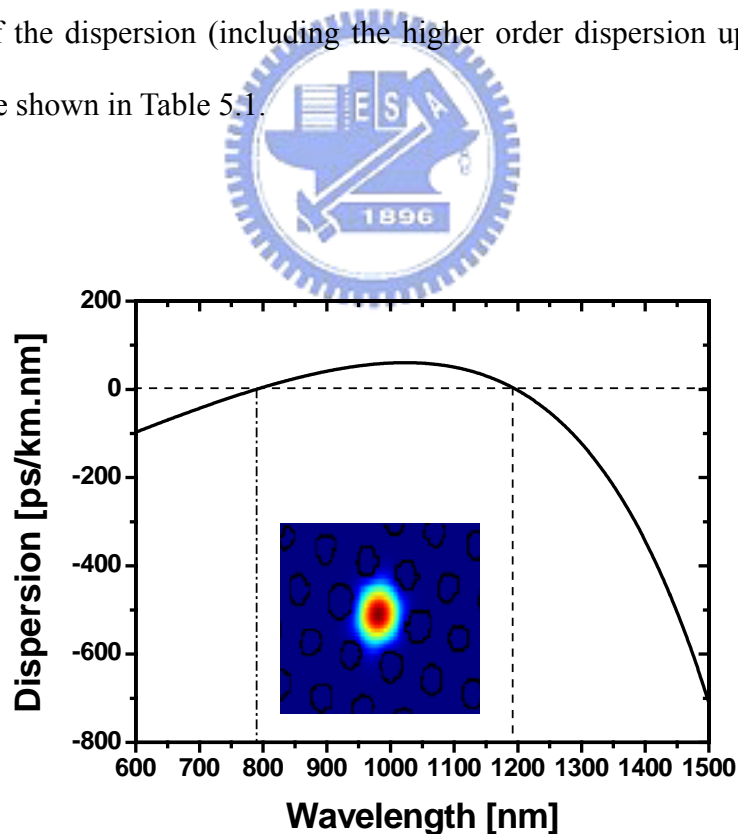

Fig. 5.1　The dispersion curve of our MF.　The two zero-dispersion points are located at 790 nm and 1190 nm.　The inset is the mode pattern of our MF.

Table 5.1   The parameters of dispersion at 1062.9 nm

$\beta 2$ (ps^2/km)	$\beta 3$ (ps^3/km)	$\beta 4$ (ps^4/km)	$\beta 5$ (ps^5/km)	$\beta 6$ (ps^6/km)
-57.79207	*-0.08328d0*	*0.00153*	*-9.20867*10^{-6}*	*5.66594*10^{-8}*

5.2 The Reliability of our Simulation: Nonlinear Schrödinger Equation

The method we used to simulate the NSE has been described in Chapter 3.   To ensure our simulation is reliable, we compared our simulation results with Ref [18]. In Ref [18], the authors simulated the contributions of various optical effects to the SC under the femtosecond pumping.   There are four circumstances the authors simulated, only SPM, SPM + SS + HOD, SPM + SS + RS and SPM + HOD + RS + SS, respectively.   The simulation results of these circumstances are shown in Fig. 5.2. Under the same simulation parameters in Table 5.2, our simulation results are also shown in Fig. 5.3 and have a good agreement with Fig. 5.2.   This indicates that our simulation of NSE is quite reliable.
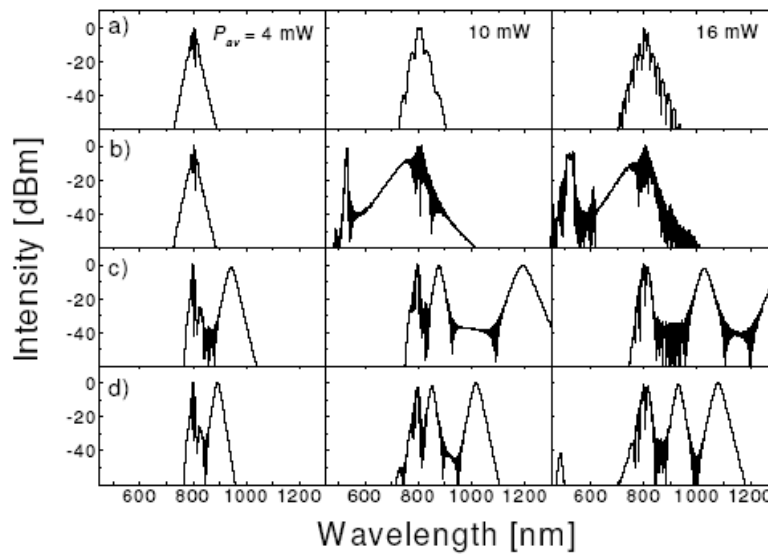

Fig. 5.2   Simulation of four circumstances in Ref [18]. a) only SPM, b) SPM + SS + HOD**,** c) SPM+SS+RS and d) SPM+HOD+RS+SS
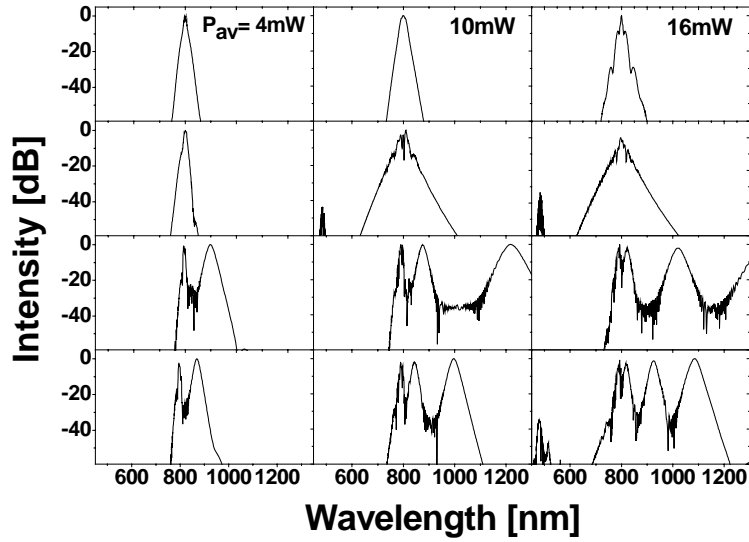
Fig. 5.3   Simulation result compared with Ref [18]. a) only SPM, b) SPM + SS + HOD, c) SPM+SS+RS and d) SPM+HOD+RS+SS
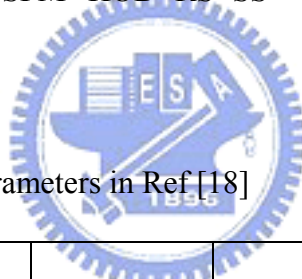
Table 5.2   The simulation parameters in Ref [18]

Pulse width	β2 (ps²/km)	β3 (ps³/km)	β4 (ps⁴/km)	β5 (ps⁵/km)	β6 (ps⁶/km)	r (/m/km)
0.1ps	-57.5	0.135	$3.12*10^{-6}$	$-2.9*10^{-7}$	$3.69*10^{-10}$	100

5.3   The Supercontinuum Spectra: Comparison of Experiment and Simulation Results

In our experiment, we first use the CML state of the Nd:GdVO₄ laser with 230 mW of average power to couple to our MF.   The output spectrum is shown in Fig. 5.3.   There are about 5 nm broadband resulted from SPM near the center.   The peak power of the CML state is only about 42 W that is not enough to generate the SC.
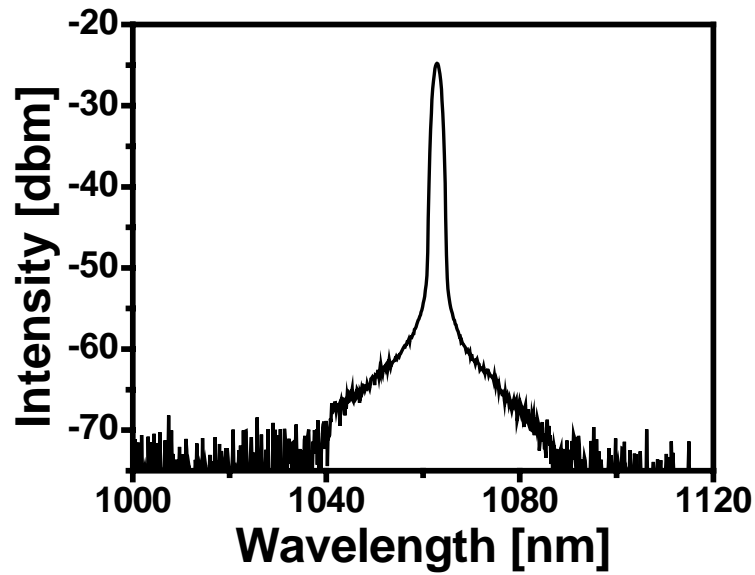
Fig. 5.4   The output spectrum generated by CML state of Nd: GdVO$_4$ laser.

In the next step, we use the QML state of Nd:GdVO$_4$ laser to couple to the MF. Under the same average power, the peak power of the QML pulse is about 14 times higher than the CML pulse.   It can induce more nonlinear effects and therefore generate the SC.   The spectrum generated by the QML pulses at 160 mW of average power is shown in Fig. 5.5.   We can find that the peak power is large enough to induce the MI even though its average power is only 160 mW.   The first Stokes and anti-Stokes components of MI are at 1081 nm and 1046 nm.   The frequency difference between the pump and the Stokes component is about 4.8 THz which is close to Ω_s = 5.28 THz (corresponding to the Stokes component at 1083 nm) calculated by the theory described in 2.1.3 with β_2 = -57.79207, γ = 74 and P_p = 430 W. The Stokes component is located within the spectrum of Raman gain and thus amplified.   The amplified Stokes component can be regarded as pumping to induce the second or the even higher Stokes component.   Therefore the spectrum shifts to the longer wavelength.   This phenomenon is also called the intrapulse Raman

31

scattering mentioned in 2.1.4. The red-shift of spectrum suppresses the gain of anti-Stokes component and result in only one anti-Stokes component on the right side of the pump.
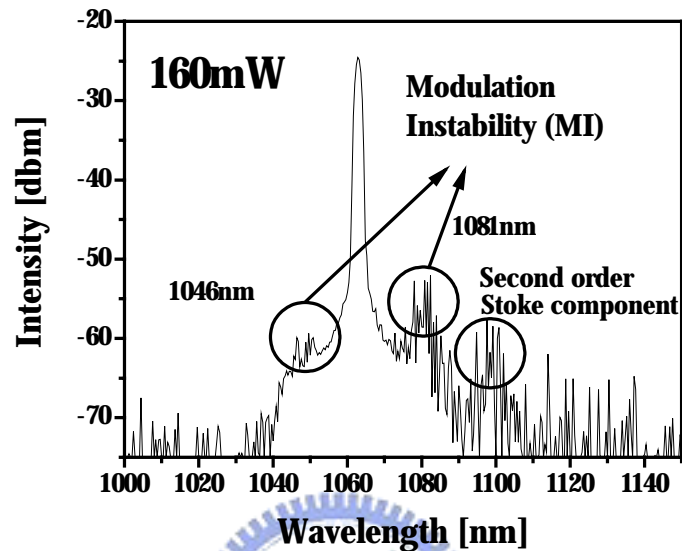

Fig. 5.5   The SC generated by QML pulses under 160 mW of average power.

Then we show the spectrum generated by QML pulses under 220 mW of average power in Fig. 5.6.   Once the red-shift spectrum exceeds the zero-dispersion point located at 1190 nm, the higher-order dispersion will disturb the spectrum and therefore generate the dispersive wave at 1315 nm.   The theory of HOD effect has mention in 2.1.6.   Compared with the spectrum generated by CML pumping in Fig. 5.4, we can get the SC from 950 nm to 1450 nm by QML pumping with average pumping power of only 220 mW.
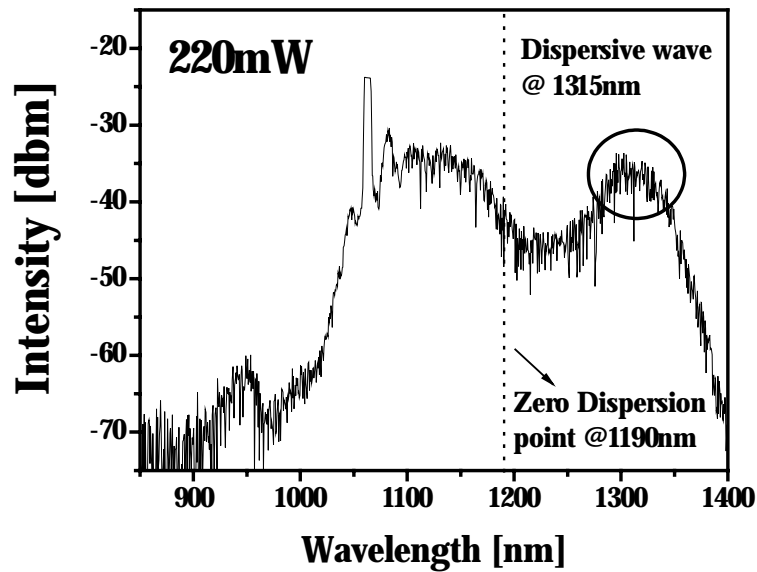
Fig. 5.6   The SC generated by QML pulses under 220 mW of average power.

Finally, we show the spectrum generated by QML pules from 160 mW to 220 mW of average power in Fig. 5.7(a) to (d).   Once the average power exceeds 230 mW, the laser system has transferred from the QML state to CML state.   Figures 5.7(e) to (h) are the corresponding simulation SC spectra.   The corresponding peak power of the experiment and the simulation is marked in Fig. 5.7.

Our simulation results [Fig. 5.7(e)-(h)] are quite similar to our experiment results. Both show the red-shift of spectrum with higher-order dispersion.   In our simulation, we sample 2^{15} points in a time window of 120 ps, giving the wavelength window from 716 to 2059 nm.   Each simulation step h is 50 μm normalized to the nonlinear interaction length and the simulated fiber length is 1 m.   However, the peak power used in the simulation is not exactly the same as the experiment.   It is because the peak power of the QML pulse in the experiment can not be measured precisely.   The noise of our simulation is a little bit high.   This may be due to the high sample points

up to 2^{15} and the effect of boundary. In the case of femtosecond pumping, the sample points are only 2^{10} and therefore there is less simulation noise in the case of picosecond pumping. Besides, the boundary condition of the simulation of NSE is the periodic boundary due to the use of the Fourier transform. Once the splitting pulse from the pump exceeds the end of the time window, it will restart shifting from the beginning of the time window and thus overlap the original signal. The original signal will be perturbed slightly and contribute to the noise in the simulation.
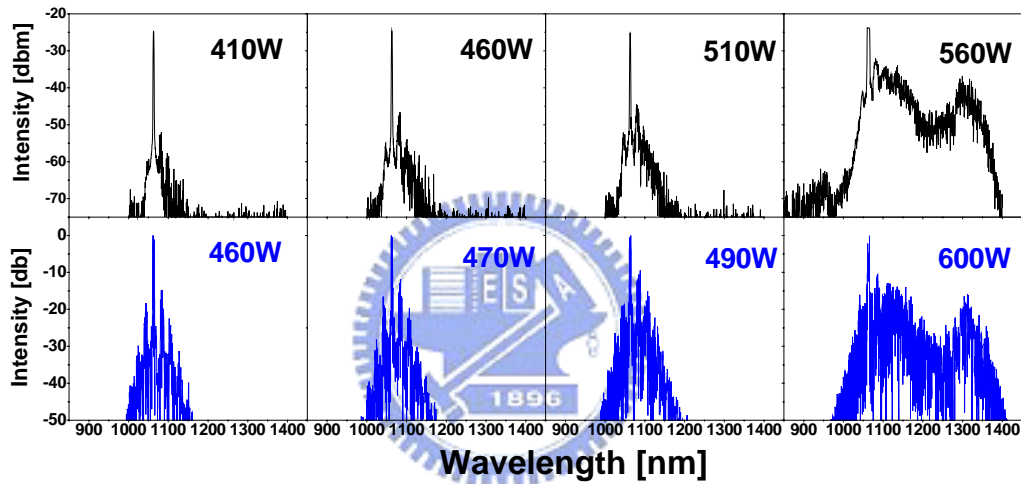

Fig. 5.7   The SC generated by QML pulse. The comparison of the experiment results (the upper row) and the simulation results (the lower row).

5.4   Numerical Results: the contribution of various optical effects to the Supercontinuum

To understand the contribution of various optical effects to the SC, we simulate four circumstances, SPM only, SPM + Raman, SPM + Raman + SS and SPM + Raman + SS +HOD, respectively, under peak power of 490 W, 600 W and 1200 W in Fig. 5.8.   If we consider only the SPM effect [Fig. 5.8(a),(e),(i)], the spectrum is

symmetrically broadened due to the MI. The contribution of SPM to the SC is limited.   Then we add the Raman effect into our simulation [Fig. 5.8(b),(f),(j)].   The peak power has exceeded the threshold of the Raman effect to shift the spectrum to the longer wavelength while the anti-Stokes components are suppressed.   Figures 5.8(c)(g)(k) contain additional nonlinear effect of SS.   The red shift of the spectrum in (c) and (g) is a little narrower than (b) and (f).   This is because of the depletion of the red shift by the SS which we have mentioned in 2.1.5.   The phenomenon of depletion in (k) will also appear at about 1900 nm.   Finally, we add the effect of higher order dispersion (HOD) to generate the dispersive wave, that agree with the experiment results.
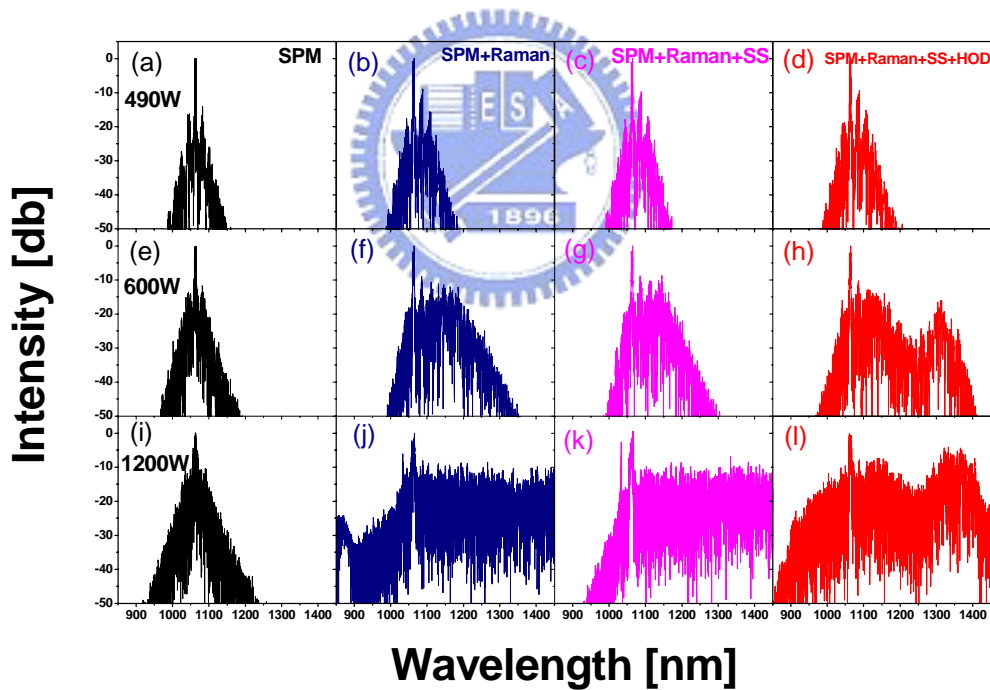

Fig. 5.8   Four circumstances of simulation: SPM only ((a),(e),(i)), SPM+Raman ((b), (f),(j)),   SPM+Raman+SS   ((c),(g),(k))   and   SPM+Raman+SS+HOD((d),(h),(i)). Upper row from (a) to (d) is the simulation of 490 W peak power while the lower rows from (e) to (h) and (i) to (l) are corresponding to 600 W and 1200 W.

Conclusion and Future Works

We have demonstrated that the QML laser can be a great pumping source which can generate the SC from 900 nm to 1400 nm in MF under the average power of 220 mW. The peak power can be enhanced to about 14 times if we change the laser system from the CML state to the QML state. The major nonlinear effects contributing to the spectrum broadening are MI, stimulated Raman scattering and the HOD effect which were also confirmed in our simulation.

In our future work, we will increase the average power of QML laser system as high as possible to test the maximum spectral broadening. The potential of the QML laser has not been unleashed completely because we only tune our laser to 220 mW. We also can use the CML laser with the same peak power of QML laser as pumping to figure out the difference of spectrum between the CML and QML pulse. Or we can double the frequency of QML pulses by KTP and couple the two kinds of QML pulses with different frequencies into the MF [40][41]. This may broaden the spectrum further. In the future work of our simulation, we can increase the speed of simulation by changing the compiler from Compaq Visual Fortran 6.6 to Intel Fortran compiler 9.0 and using the FFT function in the Intel math kernel library. The two kinds of software have been optimized to the Intel processor. We can also use Matfor to construct the interface where we can enter the parameters of input conveniently.

Appendix: Simulation of Dispersion of the Microstructured Fiber

"Mode solutions" developed by Lumerical is a powerful tool to simulate the dispersion profile of the MFs.   It is constructed by the fully-vectorial optical mode solver based on the finite difference time domain (FDTD) Yee cell.   One of the special properties of this software is the importing of SEM.   By importing the SEM of MFs, we can easily get the dispersion profile of MFs.   In the following, we will illustrate the steps how to use this software.

Step 1   Fist, we select "EDIT" tab and then "IMPORT" tab, the import dialog will appear.   This dialog contains three parts: General, Rotations and Image import.   In General, it can select the material of the fiber which is shown in Fig. A.1.   In Rotation, it can rotate the SEM to the angle we want.   In Image import, not only can import the SEM but also tune the scale of SEM after we import.   We should notice that the image size of SEM should be symmetrical, such as 638*638 pixels, or the SEM will be distorted after importing.
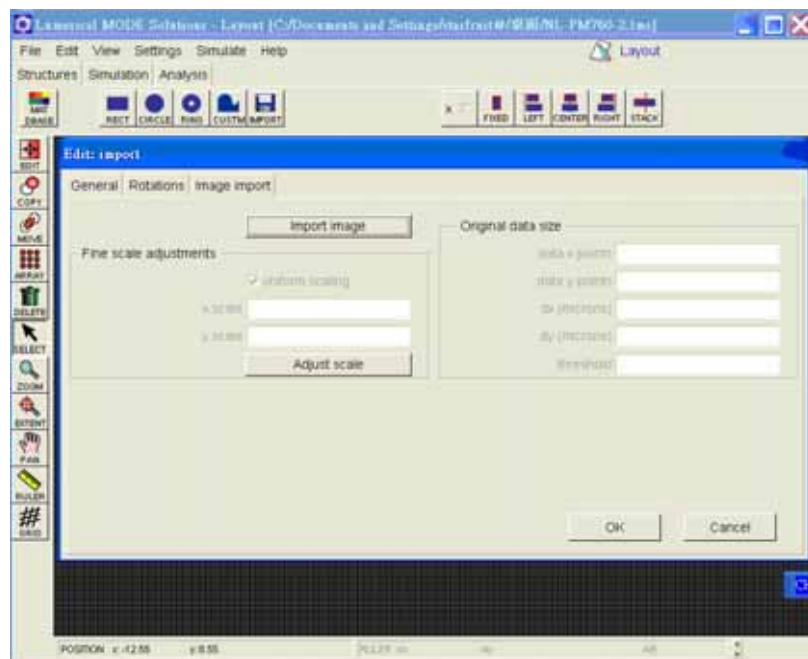

Fig. A.1   The import dialog.

Step 2   Select the material of our MF.   Usually, it is Corning 7980 Silica.
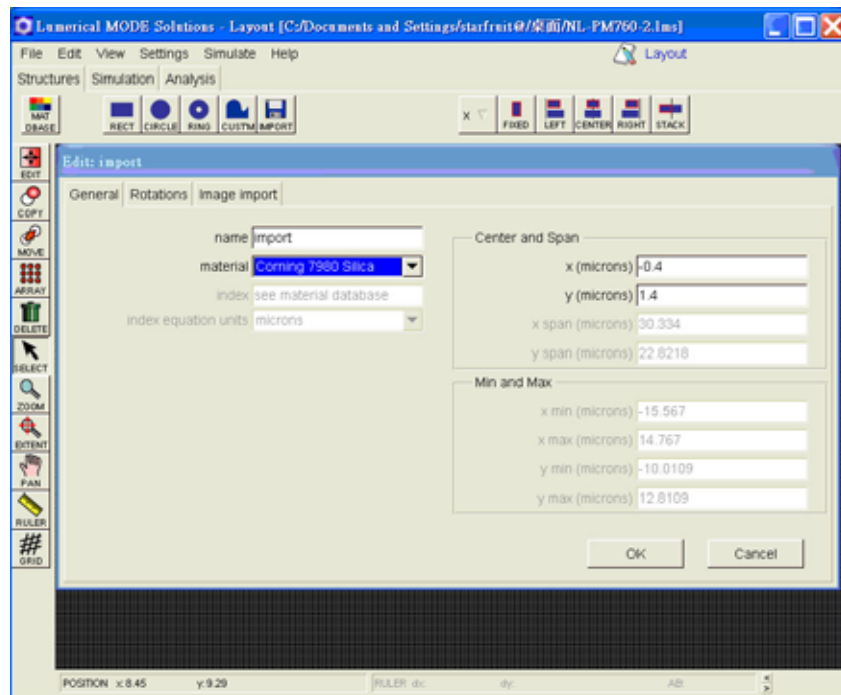

Fig. A.2   The General dialog which can select the material of the fibers

Step 3   After we select the Import image tab shown in Fig. A.1, the Image Import Wizard dialog will show up.   We can change the contrast of SEM by tuning the threshold bar.
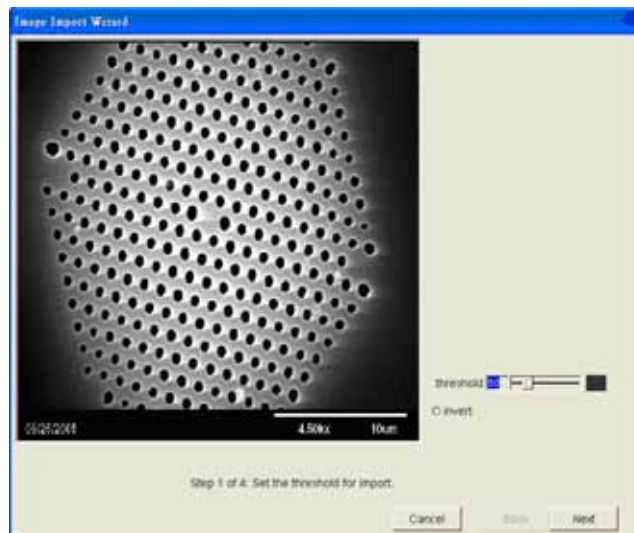

Fig A.3   The Image Import Wizard dialog

Step 4   After tuning the contrast of SEM, we should input the scale of SEM.   We

pull the mouse to define a distance of 10 microns the same as the scale shown in the SEM. In fact, the cross section of MFs will be a little distorted after taking the picture of SEM. We can adjust the input of the scale to compensate the distortion.
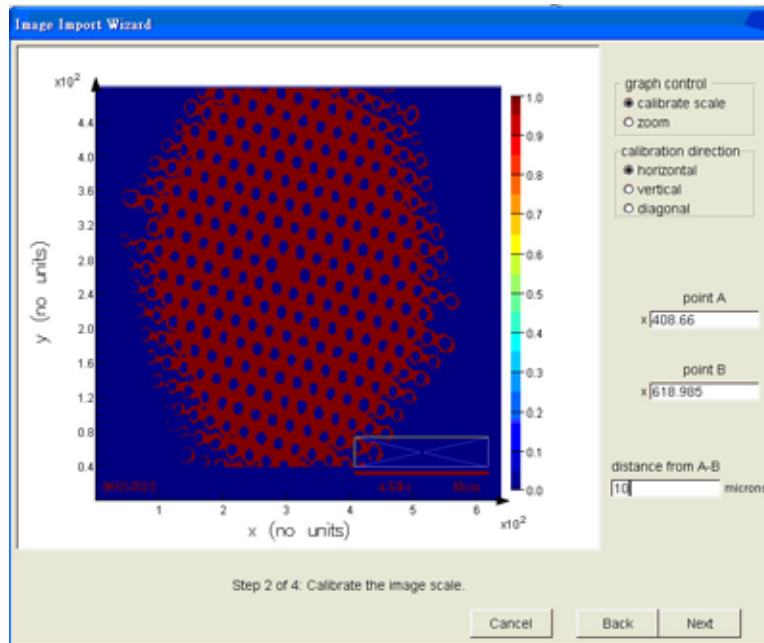

Fig A.4　Input of the scale of SEM

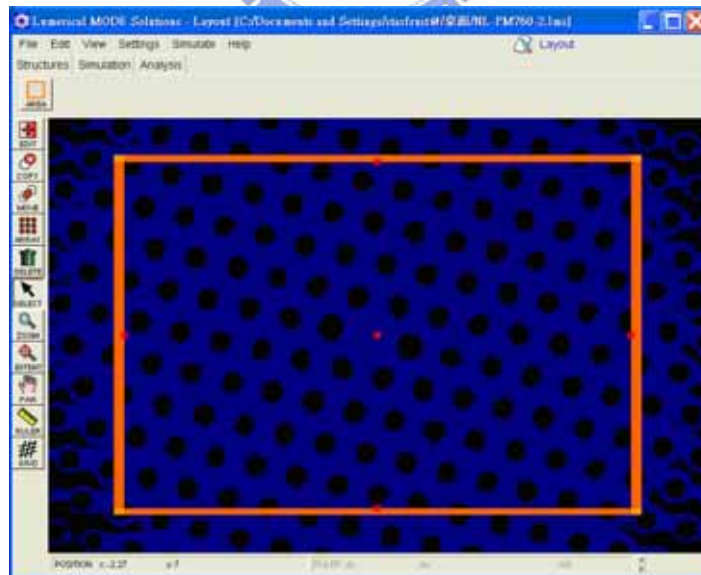**Step 5**　After importing the SEM, we should select a region to simulate.

Fig A.5　Selected region to simulate

Step 6　To select the analysis tab and to calculate the possible modes inside the MF.
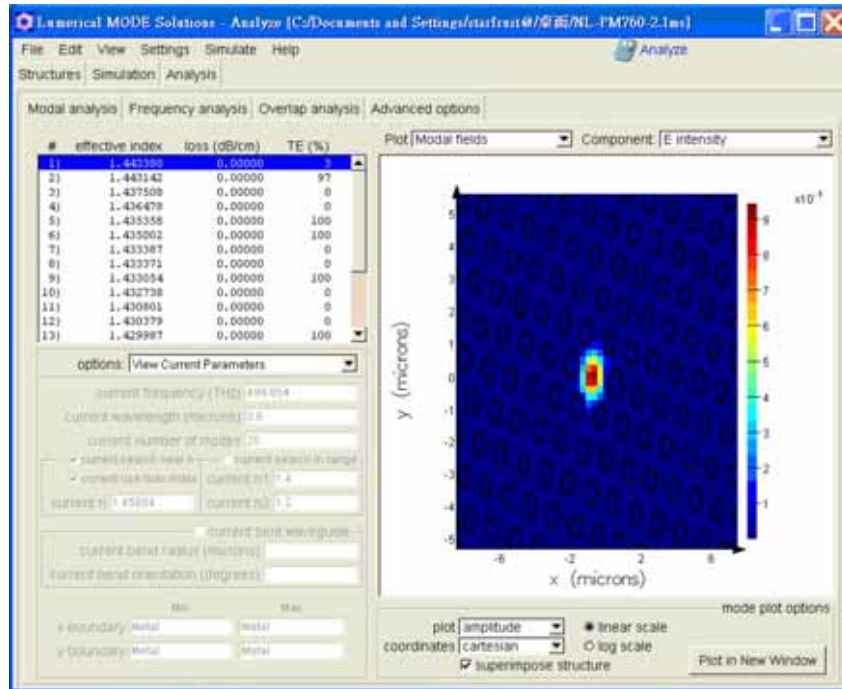
Fig A.6   Calculation of modes existing inside the MF

Step 7   After calculating the modes, we should select a mode and simulate the dispersion of the MF.   The data can be outputted to Matlab or the wordpad.
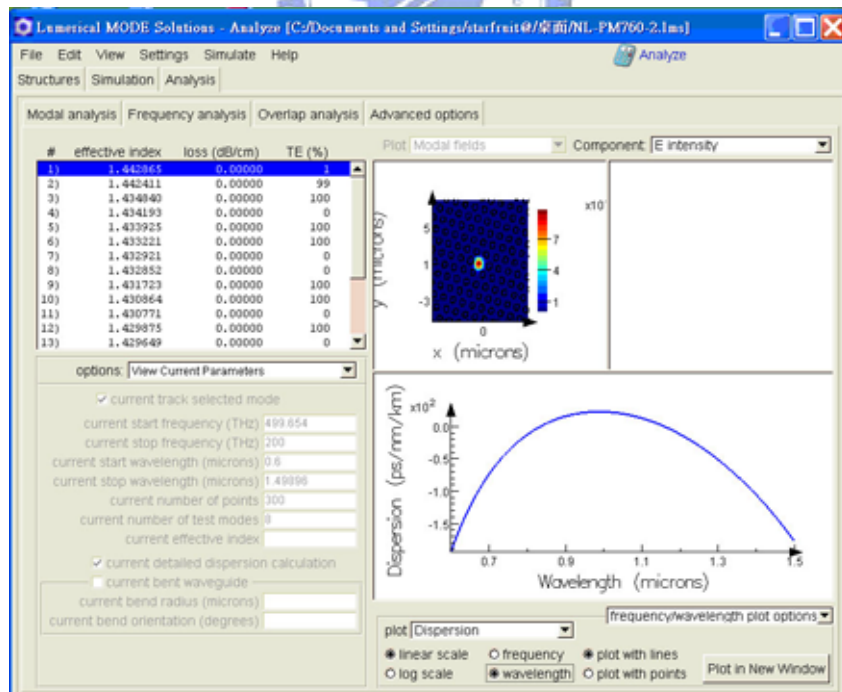

Fig A.7   Simulation of the dispersion of the MF

References

[1] P. Kaiser, E. A. J. Marcatili, and S. E. Miller, *Bell Syst. Tech. J.,* **52**, 265 (1973)

[2] T. Udem, R. Holzwarth, and T. W. Hänsch, Nature, **416**, 233 (2002).

[3] T. M. Monro, W. Belardi, K. Furusawa, J. C. Baggett, N. G. Broderick, and D. J. Richardson, *Meas. Sci. Technol.,* **12**, 854 (2001).

[4] T. Ritari, G. Genty, and H. Ludvigsen, *Opt. Lett.,* **30**, 3380, 2005

[5] Hartl, X. D. et al., *Opt. Lett.,* **26**, 608 (2001).

[6] H. Takara, T. Ohara, K. Mori, K. Sato, E. Yamada, Y. Inoue, T. Shibata, M. Abe, T. Morioka, and K-I. Sato, *Electron. Lett.,* **36**, 2089 (2000).

[7] 12. Knight, J. C., Birks, T. A., Russell, P. St. J. & Atkin, D. M., *Opt. Lett.,* **21**, 1547 (1996)

[8] Russell, P. St. J., *Science,* **299**, 358 (2003).

[9] A. Bjarklev, J. Broeng, and A. S. Bjarklev, *Photonic Crystal Fibres*, Kluwer Academic Publishers Boston (2003).

[10] J. C. Knight, J. Arriaga, T. A. Birks, A. Ortigosa-Blanch, W. J. Wadsworth, and P. S. Russell, *IEEE Photonics Technol. Lett.,* **12**, 807 (2000).

[11] A. Ferrando, E. Silvestre, P. Andres, J. J. Miret, and M. V. Andres, *Opt. Exp.,* **9**, 687 (2001).

[12] K. P. Hansen, *Opt. Exp.,* **11**, 1503 (2003).

[13] W. H. Reeves, J. C. Knight, P. S. J. Russell, and P. J. Roberts, *Opt. Exp.,* **10**, 609 (2002).

[14] R. R. Alfano and S. L. Shapiro, *Phys. Rev. Lett.,* **24**, 584 (1970).

[15] P. P. Ho, Q. X. Li, T. Jimbo, Y. L. Ku, and R. R. Alfano, *Appl. Opt.,* **26**, 2700 (1987).

[16] J. K. Ranka, R. S. Windeler, and A. J. Stentz, *Opt. Lett.,* **25**, 25 (2000).

[17] W. H. Reeves, D. V. Skryabin, F. Biancalana, J. C. Knight, P. S. Russell, F. G. Omenetto, A. Efimov, and A. J. Taylor, *Nature,* **424**, 511 (2003).

[18] G. Genty, M. Lehtonen, H. Ludvigsen, J. Broeng and M. Kaivola, *Opt. Exp.*, **10**, 1083 (2002)

[19] Michael Seefeldt*,Axel Heuer,Ralf Menzel, *Opt. Commun.,* 216 199 (2003)

[20] Stephen R., Friberg and W. Delong, *Opt. Lett.,* **17**, 979 (1992)

[21] G. P. Agrawal, *Nonlinear Fiber Optic*s, Third edition, wAcademic Press, New York (2001).

[22] F. M. Mitschke and L. F. Mollenauer, *Opt. Lett.,* **11**, 659 (1986)

[23] Nikola I. Nikolov, Thorkild Sørensen, Ole Bang and Anders Bjarklev, *J. Opt. Soc. Am. B*, **20**, 2329 (2003)

[24] Nail N. Akhmediev, Adrian Ankiewicz, *Solitons*, Chapman & Hall, Australia

[25] R. H. Stolen, and C. Lin, *Phys. Rev. A,* **17**, 1448(1978).

[26] R. H. Stolen and E. P. Ippen, *Appl. Phys. Lett.* **22**, 276 (1973)

[27] C. J. S. de Matos, K. P. Hansen, and J. R. Taylor, *Electron. Lett.,* **39**, 424 (2003)

[28] K. J. Blow, and D. Wood, *IEEE J. Quantum Electronics.,* **25**, 2665 (1989).

[29] R. H. Stolen, J. P. Gordon, W. J. Tomlinson, and H. A. Haus, *J. Opt. Soc. Am. **B** 6,* 1159 (1989)

[30] T. R. Taha and M. J. Ablowitz, *J. Comput. Phys.,* **33**, 203 (1984)

[31] R. H. Hardin and F. D. Tappert, *SIAM Rev. Chronicle*, **15**, 423 (1973)

[32] R. A. Fisher and W. K. Bischel, *Appl. Phys. Lett.,* **23**, 661 (1973)

[33] William H. Press, *Numerical Recipes in Fortran,* Second edition, Cambridge University Press (1992)

[34] Bahaa E. A. Saleh, *Fundamentals of photonics*, John Wiley & Sons, Inc.

[35] G. H. Weiss and A. A. Maradudin, *J. Math. Phys.,* **3**,771 (1962)

[36] J. A. Fleck, J. R. Morris, and M. D. Feit, *Appl. Phys.,* **10**, 129 (1962)

[37] M. Lax, J. H. Batteh, and G. P. Agrawal, *J. Appl. Phys.,* **52**, 109 (1981)

[38] Ilaria Cristiani, Riccardo Tediosi, Luca Tartara and Vittorio Degiorgio**,** *Opt. Exp.,* **12**,124 (2004)

[39] Keith J. Blow and David Wood, *IEEE J. Quantum Electronics,* **25,** 2665 (1989)

[40] Pierre-Alain Champert, Vincent Couderc, Philippe Leproux, Sébastien Février, Vincent Tombelaine, Laurent Labonté, Philippe Roy and Claude Froehly**,** *Opt. Exp.*, **12**, 4366 (2004)

[41] Vincent Tombelaine, Christelle Lesvigne, Philippe Leproux, Ludovic Grossard, Vincent Couderc, Jean-Louis Auguste, Jean-Marc Blondy**,** *Opt. Exp.*, **13**, 7399 (2005)